The Meteoritical Society

Meteoritics & Planetary Science 42, Nr 10, 1801–1816 (2007)
Abstract available online at http://meteoritics.org

Local topographic effects on photometry and reflectance spectra of planetary surfaces: An example based on lunar photometry

Deborah DOMINGUE[1*] and Faith VILAS[2†]

[1]Johns Hopkins University Applied Physics Laboratory, 11100 Johns Hopkins Road, Laurel, Maryland 20723, USA
[2]Planetary Astronomy Group, Astromaterials Research and Exploration Science,
NASA Johnson Space Center/KR, Houston, Texas 77058, USA
[†]Present address: MMT Observatory, P.O. Box 210065, The University of Arizona, Tucson, Arizona 85721–0065, USA
[*]Corresponding author. E-mail: deborah.domingue@jhuapl.edu

(Received 22 May 2006; revision accepted 19 April 2007)

Abstract–The photometric properties of the average lunar surface are characterized using Hapke's equations and whole disk observations ranging from 0.36 to 1.06 μm. Synthetic spectra across a crater topographic profile are created using the modeling results. The synthetic spectra are examined for spectral variations created by changes in lighting conditions induced by the topography. Changes above the modeling uncertainties are seen in both spectral slope and band depths, though the most pronounced change is in band depth. The data have insufficient spectral resolution to determine if there are any changes in band center due to photometric effects. No additional absorption features are introduced by the photometry. These results have serious implications on the interpretation of spectral observations in terms of abundance estimates and alteration processes as a function of location and association with geologic features.

INTRODUCTION

The purpose of remote spectral or color image observations of planetary surfaces, either from Earth-based telescopes or from spacecraft, is to determine mineralogical composition across a planet's surface. Compositional determination is made through the comparison of the observed planetary reflectance spectra with laboratory spectra of known materials, using a variety of techniques that incorporate overall background spectral shape and the attributes of absorption bands (e.g., central wavelength, band width, band area ratio, etc.). Variations in composition are mapped by the comparison of spectral or color information from one surface region to another, ratios of spectra or images, or a combination of both methods.

Mineral identification is often based on comparisons of observed planetary spectra with spectral measurements taken in the laboratory. These comparisons are often performed using various modeling techniques (Johnson et al. 1983, 1992; Mustard and Pieters 1989; Sunshine et al. 1990) in addition to direct comparisons. Mineral spectral libraries, however, generally contain laboratory measurements taken over a restricted set of viewing geometries, whereas observational spectra are taken under a variety of viewing conditions. Mineral abundance values based on these comparisons are heavily dependent on the accuracy to which the planetary observations have been corrected to the laboratory viewing conditions.

Examples of reflectance differences as a function of viewing geometry have been found in telescopic observations. Ground-based disk-integrated photometry and spectrophotometry of atmosphereless solar system bodies have shown wavelength-dependent changes in reflectance with phase (Sun-object-detector) angle. An increase in reflectance with wavelength (reddening) at wavelengths ≥0.6 μm was noted for Mercury (cf. Irvine et al. 1968), the Moon (Lane and Irvine 1973), and Vesta (Gehrels 1967) at high phase angles. Notably, Irvine et al. also observed reddening in their U-B color of Mercury at phase angle α = 70° compared to lower phase angles, also suggesting the possibility of wavelength-dependent changes with larger phase angles. Later studies of reflectance properties of the Moon also show a phase-dependent difference near 0.37 μm (Nygard 1975; S. Kronenberger, personal communication). These phase-dependent reflectance variations suggest that an accurate determination of the mineralogical composition or mineralogical variation across solar system surfaces could be altered by phase-dependent reflectance effects over the ultraviolet-visible-infrared (UV-VIS-NIR) spectral range.

Table 1. Comparative Hapke modeling results.

Hapke parameter	V[a]	V[b]	B[b]	0.50 μm
w	0.21	0.37	0.29	0.34
Bo	2.01	1	1	1
h	0.07	0.047	0.047	0.13
b	0.18	0.314	0.328	0.31
c	1	0.578	0.537	0.66
θ	20	33	33	40

[a]Helfenstein and Veverka (1987).
[b]Hartman and Domingue (1998).

The potential exists for changes in the shape of a spectral feature to be misinterpreted if the photometric effects have not been properly addressed. Compositional variations are often mapped using ratio techniques or by comparing absorption band centers and widths, often observing variations of only a few percent. Thus, compositional variations could be mimicked or hidden in observations that were poorly corrected for photometric effects.

One source of inadequately removed photometric effects stems from surface topography. The removal of photometric variations is highly dependent on the accuracy of the topographic information about the surface below. Within imaging or spectral observations, the data are often photometrically corrected to represent the dimension of the instrument footprint. Topography contained within the instrument footprint is seldom, if ever, accounted for in the photometric corrections. In many instances, localized topography is also not well accounted for in the photometric corrections. This study examines quantitatively the extent to which spectra or photometry of rocky surfaces can vary as a function of underlying topography.

A common, frequent example of local terrain excursions is provided by craters, which have slopes associated with their rims and interiors. In this study, we take a topographic profile across the lunar crater Picard obtained from the Lunar Topographic Orthophotomap (LTO-62A1 Yerkes, published by the Defense Mapping Agency) and use it to model topographic variations associated with craters at a series of latitude and longitude locations on a spherical planet of lunar size. Using these, we simulate different illumination conditions that can be associated with the resolved crater topography. We then sought a photometric data set that covered sufficient UV-VIS-NIR spectral range across sufficient phase angle variations, and was not, a priori, affected by uncorrected local topographic effects. We chose the whole disk lunar observations of Lane and Irvine (1973) taken using 8 filters from 0.36 to 1.06 μm. Using a version of the Hapke photometric model that has been demonstrated to be accurate to within <2% rms for dark lunar-like surfaces (Cheng and Domingue 2000), we modeled the Hapke parameters for each wavelength, and then created synthetic spectra for various locations along the crater profile. This provides a first-order approximation of the types of spectral variations that can be attributed to photometric effects alone, and be potentially misinterpreted as compositional variations.

Kieffer and Stone (2005) have obtained images of the Moon at 32 wavelengths, ranging from 0.35 to 2.450 μm, as part of their goal to develop a spectral radiance model of the Moon with an angular resolution and radiometric accuracy appropriate for calibrating Earth-orbiting spacecraft instrumentation. They fit their data using an empirical irradiance model now actively being used in the calibration of several Earth-orbiting spacecraft instruments, and demonstrated to track sensor response changes at the 0.1% level. These data were unpublished at the time we began our study (cf. Domingue and Vilas 2005). An extensive effort was made by Korokhin and Velikodsky (2005) to correct the Lane and Irvine data for systematic errors caused by the influence of libration variations and the different contributions of mare and highlands in integral brightness with phase changes. For our purpose of demonstrating the effects of topography on spectral characteristics, the original Lane and Irvine (1973) data are quite sufficient.

There have been many studies of lunar photometry that focus on describing various characteristics of the lunar surface, from the opposition surge (Buratti et al. 1996; Helfenstein et al. 1997; Hapke et al. 1998; Hillier et al. 1999) to microscale topography (Helfenstein and Shepard 1999). The purpose of this study is not to study the photometric behavior of the Moon further, but to examine generically how a well-understood photometric signature can vary solely as a function of viewing geometry, and what impact it could have on the interpretation of spectral characteristics. The whole-disk observations of Lane and Irvine (1973) provide a photometric signature for a generic dark surface that can be used to model spectral behavior and to quantitatively study the effect of photometry on spectral characteristics.

PREVIOUS HAPKE MODELS OF THE DISK—INTEGRATED LUNAR PHASE FUNCTION

The lunar disk-integrated solar phase curve in the Johnson V (0.55 μm) and B (0.47 μm) filters have been modeled using Hapke's equations by Helfenstein and Veverka (1987) and Hartman and Domingue (1998). The V filter phase curve modeled by Helfenstein and Veverka (1987) is derived from observations taken by Shorthill et al. (1969), Russell (1916a, 1916b), Rougier (1933), and Lane and Irvine (1973). All data were normalized to the Lane and Irvine (1973) data set and include measurements within the opposition surge (Rougier 1933). The modeling done by Helfenstein and Veverka (1987) used a Legendre polynomial for the single-particle scattering function and a different formulization of the opposition surge. Helfenstein et al. (1994) converted their modeling results into a form consistent with that described in this paper. Similarly, the V and B filter phase curves modeled by Hartman and Domingue (1998)

Table 2. Measured magnitudes of the Moon from Lane and Irvine (1973).

Date	Phase angle	0.36 μm	0.39 μm	0.46 μm	0.50 μm	0.63 μm	0.73 μm	0.86 μm	1.06 μm
30-Jul-64	76.81	–9.69	–9.94	–10.18	–10.31	–10.73	–10.91	–11.03	–11.14
24-Aug-64	21.53	–11.53	–11.74	–11.85	–11.93	–12.27	–12.42	–12.5	–12.58
24-Aug-64	22.71	–11.62	–11.78	–11.93	–12.01	–12.35	–12.48	–12.55	–12.64
25-Aug-64	33.96	–11.16	–11.36	–11.52	–11.61	–12.01	–12.16	–12.25	–12.36
25-Aug-64	35.02	–11.11	–11.28	–11.49	–11.58	–11.94	–12.1	–12.18	–12.3
30-Aug-64	100.53	–8.9	–9.1	–9.37	–9.5	–9.85	–10.04	–10.12	–10.3
21-Sep–64	6.6	–12.01	–12.17	–12.33	–12.43	–12.74	–12.88	–12.93	–13.06
22-Sep-64	16.71	–11.61	–11.77	–11.96	–12.05	–12.45	–12.6	–12.67	–12.8
17-Nov-64	24.65	–11.51	–11.65	–11.88	–11.97	–12.43	–12.56	–12.59	–12.76
18-Nov-64	10.7	–11.98	–12.12	–12.32	–12.41	–12.84	–12.97	–12.98	–13.14
9-Dec-64	118.56	–8.2	–8.39	–8.66	–8.79	–9.21	–9.45	–9.5	–9.72
12-Dec-64	83.84	–9.83	–10	–10.22	–10.32	–10.75	–10.92	–11	–11.2
9-Feb-65	83.69	–9.92	–10.13						
9–Mar–65	102.17	–9.14	–9.33	–9.52	–9.64	–10.11	–10.29	–10.35	–10.54
7-May-65	95.19	–9.44	–9.68	–9.83		–10.4	–10.53	–10.56	–10.84
8-May-65	82.11	–9.89	–10.14	–10.28	–10.38				
10-May-65	55.62	–10.75	–10.99	–11.09	–11.2	–11.68	–11.84	–11.87	–12.09
11-May-65	42.86	–11.04	–11.28	–11.39	–11.5	–11.99	–12.14	–12.19	–12.39
11-May-65	41.47	–10.94	–11.22	–11.35	–11.46	–11.97	–12.15	–12.18	–12.39
12-May-65	30.36	–11.42	–11.65	–11.74	–11.83				
12-May-65	29.23	–11.3	–11.57	–11.71	–11.82				
13-May-65	18.17	–11.77	–12.01	–12.08	–12.17	–12.61	–12.76	–12.75	–12.95
17-Jun-65	44.24	–10.87	–11.12	–11.27	–11.37	–11.84	–11.99	–12.03	–12.17
9-Jul-65	41.28	–11	–11.26	–11.43	–11.54	–12.03	–12.2	–12.25	–12.36
10-Jul-65	30.15	–11.3	–11.54	–11.71	–11.81	–12.29	–12.44		–12.58
11-Jul-65	19.17	–11.76	–11.96	–12.1	–12.21	–12.62	–12.76	–12.78	–12.89
8-Aug-65	37.51	–11.1	–11.38	–11.52	–11.62	–12.24	–12.31	–12.38	–12.48
11-Aug-65	6.62	–12	–12.23	–12.37	–12.46	–12.98	–13.06	–13.06	–13.21
14-Sep-65	47.74	–10.91	–11.13	–11.27	–11.36	–11.83	–11.96	–12.01	–12.15
11-Oct-65	17.23	–11.72	–11.94	–12.05	–12.14	–12.61	–12.73	–12.76	–12.87
12-Oct-65	29.27	–11.34	–11.56	–11.68	–11.77	–12.28	–12.42	–12.44	–12.57
7-Nov-65	15.65					–12.69	–12.84	–12.87	–12.98

include data from Russell (1916a), Rougier (1933), and Lane and Irvine (1973), which also include opposition measurements (Rougier 1933). Each group made slightly different assumptions in their modeling. The results are shown in Table 1 along with the 0.50 μm modeling results from this study for comparison. The 0.50 μm results are consistent with the Hartman and Domingue (1998) V filter results, which use similar modeling assumptions.

DISK-INTEGRATED DATA ANALYSIS

Data Preparation

In order to keep the database self-contained, this study used the values derived for the solar magnitude and solar phase curves of the full Moon by Lane and Irvine (1973). The Lane and Irvine (1973) observations were made using a suite of 10 narrowband filters between 0.32 and 1.06 μm, and in the broadband Johnson UBV filters, as part of a larger program to obtain photoelectric photometry of the larger planets. Two aspects of these lunar observations are significant. First, the observations cover phase angles from 6° through 120°. More importantly, the observers used a special f/15 fused quartz lens 20 mm in diameter constructed solely for this study. The lens reduced the whole lunar image in the focal plane to a size comparable to the planets observed as part of the same program. This image was fed directly into the photometer. For the purposes of this study we used the observed magnitude of the Moon in eight of the nine narrowband filters, as shown in Table 2. We did not use the 0.42 μm observations since we did not obtain an adequate Hapke model solution to this data set.

The observed magnitudes shown in Table 2 were converted to absolute magnitude, M_a, using the relationship:

$$M_a = M_o - M_{sun} - 5\log\left(\frac{Dr}{sR}\right) \quad (1)$$

where M_o is the observed lunar magnitude, M_{sun} is the solar magnitude, D is the Earth-Moon distance, r is the Moon-Sun distance, s is the Earth-Sun distance, and R is the lunar radius. The individual solar magnitudes for each filter wavelength, listed in Table 3, were derived from the equation for the geometric albedo of the full Moon:

$$\log p = 0.4\lfloor M_{sun} - M_{full} \rfloor - 2\log(\sin\sigma) \quad (2)$$

Table 3. Solar magnitudes.

Wavelength	0.36 μm	0.39 μm	0.46 μm	0.50 μm	0.63 μm	0.73 μm	0.86 μm	1.06 μm
Solar magnitude	–26.8102	–26.81	–26.8055	–26.8103	–26.8098	–26.8114	–26.8114	–26.8102

as given in Lane and Irvine (1973). In this equation, p is the geometric albedo, M_{sun} is the solar magnitude, M_{full} is the magnitude of the Moon at full Moon, and $\sigma = 0.0045216$, which is the angular radius of the Moon at the mean Earth-Moon distance. The values of p calculated by Lane and Irvine (1973) are derived from values of the lunar magnitude at full Moon based on a linear extrapolation of the 1965 data set that excludes the opposition effect. The absolute magnitudes of the Moon were converted to I/F reflectance values, which are listed in Table 4, using the standard relationship $I/F = 10^{-0.4M}$.

Model

The Lane and Irvine (1973) disk-integrated observations were modeled using Hapke's equations (Hapke 1981, 1984, and 1986). In these equations, the absolute reflectance is given as:

$$\frac{I}{F} = \left(\frac{w}{8}\{[1 + B(\alpha)]P(\alpha) - 1\} + \frac{r_o}{2}(1 - r_o)\right) \quad (3)$$
$$\left\{1 - \sin\left(\frac{\alpha}{2}\right)\tan\left(\frac{\alpha}{2}\right)\ln\left[\cot\left(\frac{\alpha}{4}\right)\right]\right\} +$$
$$\frac{2}{3}r_o^2\left(\frac{\sin(\alpha) + (\pi - \alpha)\cos(\alpha)}{\pi}\right)S(\alpha, \theta)$$

where w is the single scattering albedo, α is the solar phase angle, and θ is the surface roughness parameter. The term r_o is given by:

$$r_o = \frac{1 - \sqrt{1 - w}}{1 + \sqrt{1 - w}} \quad (4)$$

and the opposition effect term, $B(\alpha)$ is given by:

$$B(\alpha) = \frac{B_o}{1 + \frac{\tan(\alpha/2)}{h}} \quad (5)$$

where B_o describes the amplitude of the opposition effect and h describes the width of the opposition peak. Since the Lane and Irvine (1973) data only go down to 6° solar phase, these parameters are poorly constrained by the data set. The single particle scattering function used in the model is a double Henyey-Greenstein function of the form:

$$P(\alpha) = \frac{(1 - c)(1 - b^2)}{[1 - 2b\cos\alpha + b^2]^{3/2}} + \frac{c(1 - b^2)}{[1 + 2b\cos\alpha + b^2]^{3/2}} \quad (6)$$

where b describes the amplitude of the scattering peaks and c describes the relative abundance of forward to backward scattering. The term $S(\alpha,\theta)$ is a correction term for surface roughness, where the surface roughness parameter, θ, is defined as the average slope over the resolution element of the detector (Hapke 1984). The term $S(\alpha,\theta)$, as provided in Hapke (1986) and used here, overestimates surface roughness at phase angles greater than 60°. However, Cheng and Domingue (2000) have shown that the Hapke model using this term can accurately model and predict reflectance values (to within 2% for dark albedo surfaces) at phase angles greater than 60° using this term. It is the predictive nature of the Hapke model that is needed for this study.

A revised and updated Hapke model (Hapke 2002) exists that incorporates an opposition surge element due to coherent backscatter and has an additional term for multiple scattering. This model was not used since the data being modeled do not describe the opposition surge well, and thus cannot constrain the additional parameters well in the revised model. The Hapke model equations used in this study (Hapke 1986) have been shown to estimate photometric behavior to within 2% (Cheng and Domingue 2000). A similar study of the estimation capabilities of the revised model has not been completed. The purpose of this study is to examine spectral reflectance changes. Thus, a model is needed that can accurately estimate reflectance values for a set of viewing geometries. The Hapke equations used here have been demonstrated to provide this estimation capability within sufficient accuracy (Cheng and Domingue 2000) and are used for the purposes of this study.

The absolute reflectance values derived from the Lane and Irvine (1973) lunar observations were fit with the Hapke equations using a least squares grid search over the Hapke parameter space, using an algorithm described by Domingue et al. (1997, 2002). The least squares routine minimizes χ and can vary all parameters simultaneously. The value of χ is defined as:

$$\chi = \sqrt{\frac{\sum(R_{obs} - R_{cal})^2}{N}} \quad (7)$$

where R_{obs} is the observed disk-integrated reflectance (taken from Table 4), R_{cal} is the calculated disk-integrated reflectance from the Hapke model, and N is the number of data points. No constraints were placed on any of the parameters other than they are not allowed to vary outside of physical meaningful values as defined by the model. Even if

Table 4. Absolute reflectance of the Moon.

Date	Phase angle	0.36 μm	0.39 μm	0.46 μm	0.50 μm	0.63 μm	0.73 μm	0.86 μm	1.06 μm
30-Jul-64	76.81	0.0069	0.0087	0.0109	0.0123	0.0181	0.0213	0.0238	0.0264
24-Aug-64	21.53	0.0378	0.0459	0.0510	0.0546	0.0747	0.0857	0.0922	0.0994
24-Aug-64	22.71	0.0411	0.0476	0.0549	0.0588	0.0804	0.0905	0.0966	0.1050
25-Aug-64	33.96	0.0269	0.0323	0.0376	0.0407	0.0588	0.0674	0.0733	0.0812
25-Aug-64	35.02	0.0257	0.0300	0.0366	0.0396	0.0551	0.0638	0.0687	0.0768
30-Aug-64	100.53	0.0034	0.0040	0.0052	0.0058	0.0080	0.0096	0.0103	0.0122
21-Sep-64	6.6	0.0588	0.0681	0.0793	0.0866	0.1152	0.1309	0.1370	0.1547
22-Sep-64	16.71	0.0407	0.0471	0.0564	0.0610	0.0882	0.1011	0.1079	0.1217
17-Nov-64	24.65	0.0371	0.0422	0.0524	0.0567	0.0866	0.0975	0.1002	0.1173
18-Nov-64	10.7	0.0572	0.0651	0.0786	0.0850	0.1263	0.1422	0.1435	0.1665
9-Dec-64	118.56	0.0018	0.0021	0.0027	0.0030	0.0045	0.0056	0.0058	0.0071
12-Dec-64	83.84	0.0079	0.0092	0.0114	0.0124	0.0184	0.0215	0.0232	0.0279
9-Feb-65	83.69								
9-Mar-65	102.17	0.0086	0.0104						
7-May-65	95.19	0.0042	0.0050	0.0060	0.0066	0.0102	0.0120	0.0127	0.0152
8-May-65	82.11	0.0055	0.0069	0.0079	0.0000	0.0134	0.0150	0.0154	0.0200
10-May-65	55.62	0.0083	0.0105	0.0120	0.0131				
11-May-65	42.86	0.0184	0.0230	0.0253	0.0279	0.0434	0.0502	0.0516	0.0633
11-May-65	41.47	0.0241	0.0300	0.0334	0.0368	0.0577	0.0662	0.0693	0.0834
12-May-65	30.36	0.0219	0.0284	0.0322	0.0354	0.0567	0.0668	0.0687	0.0834
12-May-65	29.23	0.0341	0.0422	0.0460	0.0498				
13-May-65	18.17	0.0306	0.0392	0.0448	0.0494				
17-Jun-65	44.24	0.0471	0.0588	0.0630	0.0681	0.1022	0.1172	0.1161	0.1398
9-Jul-65	41.28	0.0206	0.0259	0.0299	0.0326	0.0503	0.0577	0.0598	0.0681
10-Jul-65	30.15	0.0232	0.0295	0.0346	0.0381	0.0599	0.0700	0.0733	0.0812
11-Jul-65	19.17	0.0306	0.0381	0.0448	0.0489	0.0761	0.0873	0.0000	0.0994
8-Aug-65	37.51	0.0467	0.0562	0.0642	0.0707	0.1032	0.1172	0.1194	0.1322
11-Aug-65	6.62	0.0254	0.0329	0.0376	0.0410	0.0727	0.0774	0.0826	0.0906
14-Sep-65	47.74	0.0583	0.0720	0.0823	0.0890	0.1437	0.1545	0.1545	0.1776
11-Oct-65	17.23	0.0213	0.0261	0.0299	0.0323	0.0498	0.0561	0.0587	0.0669
12-Oct-65	29.27	0.0450	0.0551	0.0613	0.0663	0.1022	0.1140	0.1172	0.1298
7-Nov-65	15.65	0.0317	0.0389	0.0436	0.0471	0.0754	0.0857	0.0873	0.0985

Table 5. Hapke parameter values for the Moon.

Wavelength	0.36 μm	0.39 μm	0.46 μm	0.50 μm	0.63 μm	0.73 μm	0.86 μm	1.06 μm
w	0.37	0.33	0.39	0.34	0.66	0.69	0.69	0.77
B_o	0.11	1	0.86	1	0.6	0.56	0	0.23
h	0.8	0.26	0.18	0.13	0.37	0.41		0.8
b	0.52	0.39	0.41	0.31	0.59	0.57	0.63	0.63
c	0.87	0.83	0.83	0.66	0.94	0.93	0.91	0.94
θ	40	40	40	40	40	40	35	40
χ	0.001932	0.002608	0.002414	0.003087	0.002261	0.007268	0.009951	0.007999

Error bars: $w = \pm 0.04$, $B_o = \pm 0.3$, $h = \pm 0.1$, $b = \pm 0.04$, $c = \pm 0.08$, $\theta = \pm 5°$.

the parameter value hits a limit, the fitting algorithm does a finite "reset" to explore a larger portion of the parameter space. Table 5 lists the resulting Hapke parameter values and the corresponding χ values for each fit.

Modeling Results

The Hapke model fits to the lunar data set are plotted in Fig. 1; the corresponding values for the parameters are in Table 5. The Hapke parameter value error bars are based on the grid size of the least-squares grid search and the range of solar phase angles in the data set. For example, since there are no data below 6°, the opposition parameters are poorly constrained; this is reflected in the error bar values for B_o and h.

TOPOGRAPHY AND PHOTOMETRY

Crater Topographic Modeling

The incidence (i) and emission (e) angles on a spherical body can be defined in terms of luminance coordinates, where the luminance equator is the great circle on the surface

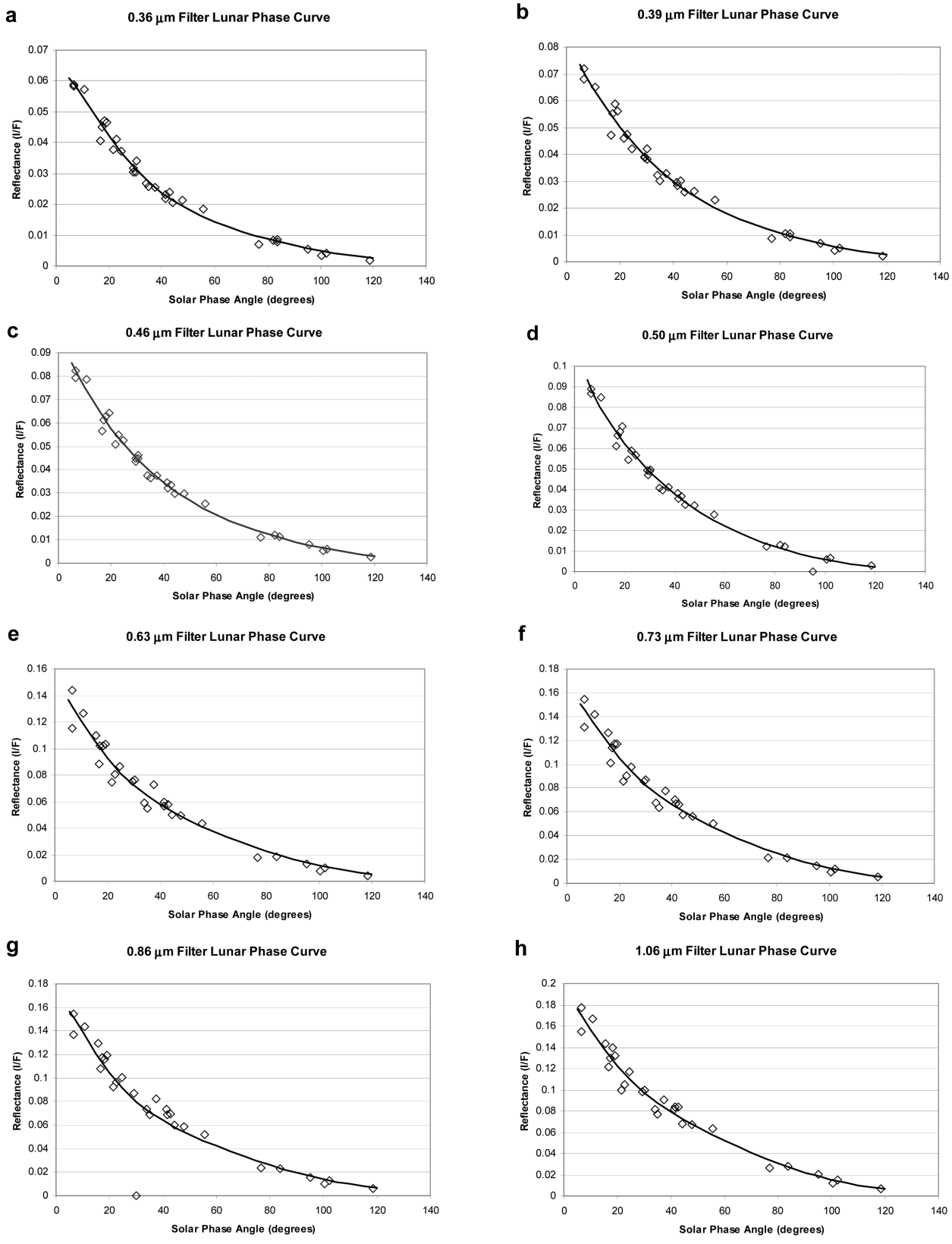

Fig. 1. Lunar phase curves at (a) 0.36 μm, (b) 0.39 μm, (c) 0.46 μm, (d) 0.50 μm, (e) 0.63 μm, (f) 0.73 μm, (g) 0.86 μm, and (h) 1.06 μm as measured by Lane and Irvine (1973) are plotted in diamonds. The Hapke model fits corresponding to the parameters listed in Table 5 are shown by the solid lines.

containing the sub-observer and sub-solar points. This does not necessarily correspond to the geographical equator unless the sub-observer and sub-solar points also fall on the geographical equator. Lines of luminance longitude (Λ) fall on great circles perpendicular to the luminance equator, and luminance latitude (L) is defined as the angular distance from the luminance equator along a great circle perpendicular to the luminance equator. The solar phase angle (α) is the angular distance between the sub-observer and sub-solar points. These relationships and definitions are illustrated in Fig. 2. Using the law of cosines for spherical triangles, the values for the incidence and emission angles for a point on the spherical planet are given by:

$$\cos(i) = \cos(\Lambda + \alpha)\cos(L) \tag{8}$$

and

$$\cos(e) = \cos(\Lambda)\cos(L) \tag{9}$$

Thus for any point on the surface, for a given illumination and observing geometry, values of i and e can be derived. For a point on the surface, an x-y-z coordinate system can be specified such that the x-z plane is defined as the plane containing the surface normal and the incidence angle. Furthermore, the z-axis can be further constrained to be coincident with the surface normal. In such a coordinate system, unit vectors along the incidence and emission directions are given by:

$$\hat{I} = \sin(i)\hat{i} + \cos(i)\hat{k} \tag{10}$$

and

$$\hat{E} = \sin(e)\cos(\alpha_p)\hat{i} + \sin(e)\sin(\alpha_p)\hat{j} + \cos(e)\hat{k} \tag{11}$$

respectively, where α_p is the solar phase angle projected onto the x-y plane. The value of α_p is given by:

$$\alpha_p = \arccos\left[\frac{\cos(\alpha) - \cos(i)\cos(e)}{\sin(i)\sin(e)}\right] \tag{12}$$

To account for local topography at a point on a spherical planet, an actual surface normal vector can be defined by two angles: β, which is the angle in the x-z plane between the surface normal and the actual normal; and γ, which is the angle rotated from the x-z plane toward the +y-axis direction of the actual normal. This is illustrated in Fig. 3. The unit vector in the direction of the actual normal is given by:

$$\hat{n} = \sin(\beta)\cos(\gamma)\hat{i} + \sin(\beta)\sin(\gamma)\hat{j} + \cos(\beta)\hat{k} \tag{13}$$

The actual incidence and emission angles (i_a and e_a, respectively) are defined as the angle between the actual surface normal and the incidence and emission angles, respectively. The values for i_a and e_a are given by the following relationships:

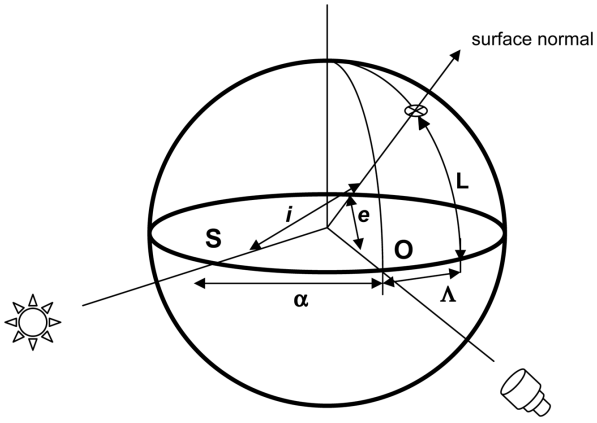

Fig. 2. The luminance coordinate system. S is the sub-solar point and O is the sub-observer point, which are separated by a solar phase angle of α. The circled x marks an arbitrary point on the surface of the sphere at a luminance longitude Λ and a luminance latitude L. Luminance coordinates are independent of geographical coordinates.

$$\hat{n} \bullet \hat{I} = \cos(i_a) \tag{14}$$
$$\cos(i_a) = \sin(i)\sin(\beta)\cos(\gamma) + \cos(i)\cos(\beta)$$

and

$$\hat{n} \bullet \hat{E} = \cos e_a \cos(e_a) = \tag{15}$$
$$\sin(e)\cos(\alpha_p)\sin(\beta)\cos(\gamma) + \sin(e)\sin(\alpha_p)$$
$$\sin(\beta)\sin(\gamma) + \cos(e)\cos(\beta)$$

To study the effects of topography, we have taken a profile along the lunar crater Picard from the LTO-62A1. Figure 4a shows the profile taken across the crater, while Table 6 lists the distance, altitude, and slope values along the profile. Corresponding normal vectors along the profile were calculated. We examined several orientations of the profile. The first orientation places the profile in the x-z plane, with values for β corresponding to the slopes and a nominal value of $\gamma = 0$. Subsequent orientations of the profile have values for β corresponding to the slopes and values of γ of 60, 90, 130, and 180 degrees.

The value of β is given by:

$$\beta = \frac{\pi}{2} - \arctan\left(\frac{\Delta x}{\Delta y}\right) \tag{16}$$

where Δx is defined as the distance between two segments along the profile, and Δy is the difference in altitude from the beginning to the end of the segment.

In our analyses, the following simplifying assumptions were made:

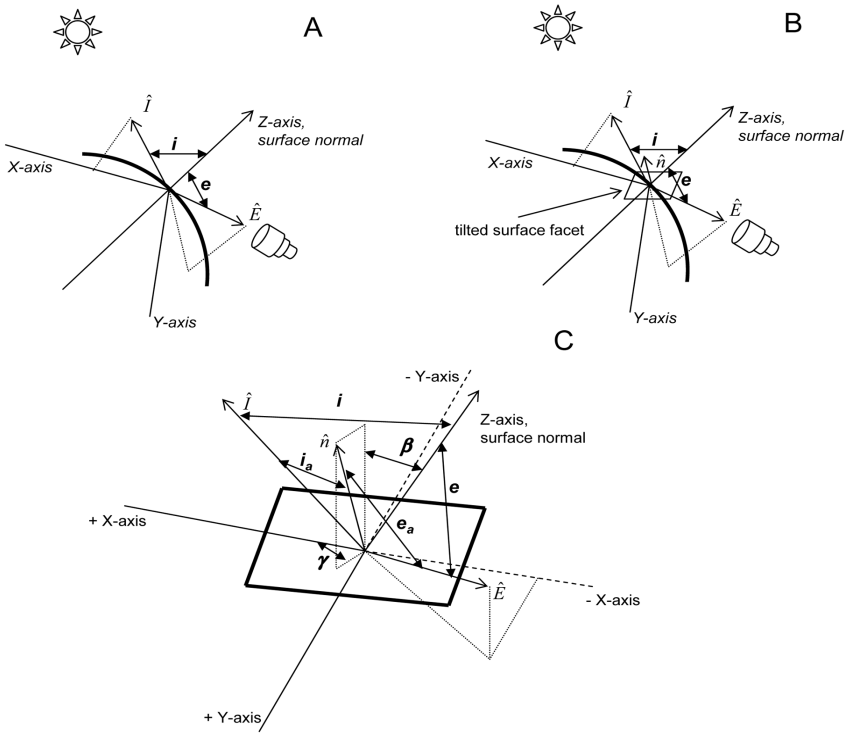

Fig. 3. Geometry accounting for local topography. a) The local coordinate system for an arbitrary point on the surface of a spherical planet. b) The relationship between the coordinate system established in (a) to a tilted, topographic surface with an actual surface normal, $\hat{n}$. c) The relationship between the coordinate system and the photometric angles described in the text. The actual incident and emission angles, i_a and e_a, respectively, along with the solar phase angle, are the angles required to calculate the surface reflectance for topographic features.

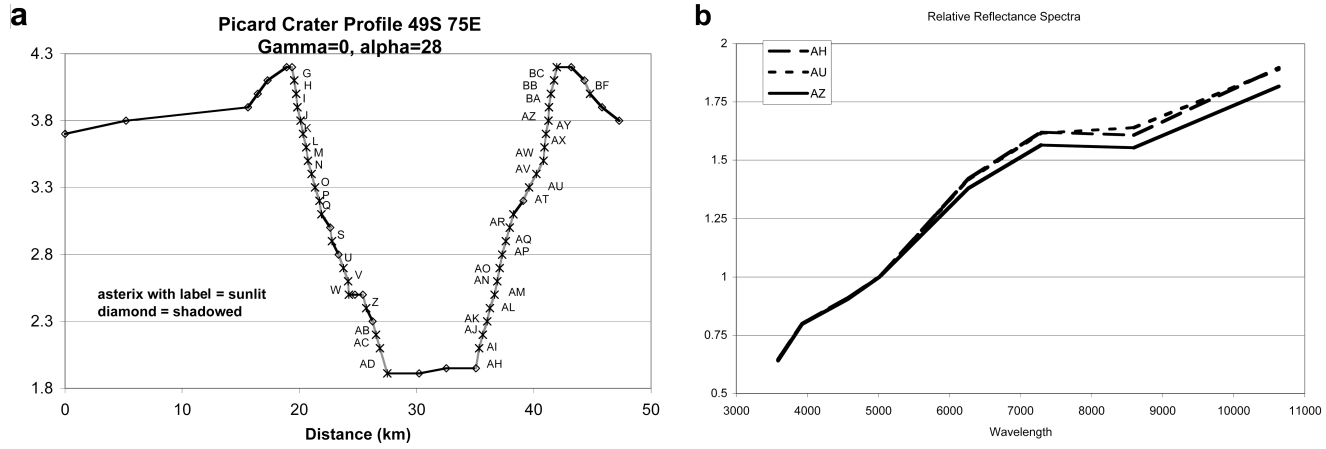

Fig. 4. a) The crater profile at 49° latitude, 75° longitude, and an orientation with γ = 0 is shown, where the sunlit segments are labeled and marked by an asterisk. b) Synthetic spectra, normalized to 1 at 0.50 μm, are plotted for example segments that show shallow (segment AU, dotted line), deep (segment AZ, solid line), and average (segment AH, dashed line) band depths at 0.86 μm.

- The geographic equator and luminance equator are equivalent.
- The profiles were placed at three separate latitudes (49S, 67S, and 80S).
- For each latitude, we assumed longitude values of 10, 50, 75, and 85 degrees.
- We looked at a solar phase angle of 28 degrees.

The angle equations are simplified by assuming that the geographic and luminance equators are equivalent. Offsets in these two equators could be compensated for by changing the latitude and longitude of the profile. The purpose of this study is to demonstrate whether spectral variations can be induced by viewing angle, and these assumptions test an adequate range of physically viable viewing geometries.

Reflectance Modeling

Hapke's equations (Hapke 1984) for disk-resolved reflectance of a rough surface assumes that the reflectance for a rough surface (r_R) can be given by the reflectance for a smooth surface (r_s) plus a multiplicative factor (S), or:

$$r_R(i, e, \alpha) = r_s(i, e, \alpha)S(i, e, \alpha, \theta) \quad (17)$$

where θ is the average surface tilt within the detector's footprint resolution. In this formalism, a reference surface can be defined where i and e are relative to the surface normal of the reference surface. If this reference surface is actually a series of faceted and tilted surfaces (i.e., a rough surface), then incident and emission angles relative to the normal of the tilted surfaces, i′ and e′, respectively, can be defined such that their relationship to the reference surface are given by:

$$\cos(i') = \mu'_0 = \frac{1}{\sqrt{1 + \pi\tan^2}} \quad (18)$$

$$\left[\cos i + \sin i \tan\theta \frac{\cos(\Psi)e^{\left(\frac{-\cot^2\theta\cot^2 e}{\pi}\right)} + \sin^2\left(\frac{\Psi}{2}\right)e^{\left(\frac{-\cot^2\theta\cot^2 i}{\pi}\right)}}{2 - e^{\left(-\frac{2}{\pi}\cot\theta\cot e\right)} - \frac{\Psi}{\pi}e^{\left(-\frac{2}{\pi}\cot\theta\cot i\right)}}\right]$$

$$\cos(e') = \mu' = \frac{1}{\sqrt{1 + \pi\tan^2\theta}}$$

$$\left[\cos e + \sin e \tan\theta \frac{e^{\left(\frac{-\cot^2\theta\cot^2 e}{\pi}\right)} - \sin^2\left(\frac{\Psi}{2}\right)e^{\left(\frac{-\cot^2\theta\cot^2 i}{\pi}\right)}}{2 - e^{\left(-\frac{2}{\pi}\cot\theta\cot e\right)} - \frac{\Psi}{\pi}e^{\left(-\frac{2}{\pi}\cot\theta\cot i\right)}}\right]$$

when i ≤ e and by:

$$\cos(i') = \mu'_0 = \frac{1}{\sqrt{1 + \pi\tan^2\theta}} \quad (19)$$

$$\left[\cos i + \sin i \tan\theta \frac{e^{\left(\frac{-\cot^2\theta\cot^2 i}{\pi}\right)} - \sin^2\left(\frac{\Psi}{2}\right)e^{\left(\frac{-\cot^2\theta\cot^2 e}{\pi}\right)}}{2 - e^{\left(-\frac{2}{\pi}\cot\theta\cot i\right)} - \frac{\Psi}{\pi}e^{\left(-\frac{2}{\pi}\cot\theta\cot e\right)}}\right]$$

$$\cos(e') = \mu' = \frac{1}{\sqrt{1 + \pi\tan^2\theta}}$$

Table 6. Distance versus altitude along crater profile.

Distance (km)	Altitude (km)	Slope	Distance (km)	Altitude (km)	Slope
0	3.7		30.2	1.912	0.000
5.21	3.8	0.019	32.5	1.95	0.017
15.6	3.9	0.010	35.1	1.95	0.000
16.5	4	0.111	35.3	2.1	0.750
17.3	4.1	0.125	35.6	2.2	0.333
18.9	4.2	0.063	36	2.3	0.250
19.4	4.2	0.000	36.3	2.4	0.333
19.6	4.1	–0.500	36.6	2.5	0.333
19.7	4	–1.000	36.9	2.6	0.333
19.8	3.9	–1.000	37.1	2.7	0.500
20.1	3.8	–0.333	37.3	2.8	0.500
20.3	3.7	–0.500	37.6	2.9	0.333
20.6	3.6	–0.333	37.9	3	0.333
20.7	3.5	–1.000	38.3	3.1	0.250
21	3.4	–0.333	39.1	3.2	0.125
21.3	3.3	–0.333	39.6	3.3	0.200
21.7	3.2	–0.250	40.2	3.4	0.167
21.9	3.1	–0.500	40.8	3.5	0.167
22.6	3	–0.143	40.9	3.6	1.000
22.8	2.9	–0.500	41	3.7	1.000
23.3	2.8	–0.200	41.3	3.8	0.333
23.8	2.7	–0.200	41.4	3.9	1.000
24.1	2.6	–0.333	41.5	4	1.000
24.2	2.5	–1.000	41.7	4.1	0.500
24.7	2.5	0.000	42	4.2	0.333
25.4	2.5	0.000	43.2	4.2	0.000
25.7	2.4	–0.333	44.3	4.1	–0.091
26.3	2.3	–0.167	44.8	4	–0.200
26.5	2.2	–0.500	45.8	3.9	–0.100
26.9	2.1	–0.250	47.3	3.8	–0.067
27.5	1.912	–0.313			

$$\left[\cos e + \sin e \tan\theta \frac{\cos(\Psi)e^{\left(\frac{-\cot^2\theta\cot^2 i}{\pi}\right)} + \sin^2\left(\frac{\Psi}{2}\right)e^{\left(\frac{-\cot^2\theta\cot^2 e}{\pi}\right)}}{2 - e^{\left(-\frac{2}{\pi}\cot\theta\cot i\right)} - \frac{\Psi}{\pi}e^{\left(-\frac{2}{\pi}\cot\theta\cot e\right)}}\right]$$

when $i > e$. In these equations θ is defined as the average angular tilt of the surfaces and Ψ is the azimuth angle which is given by:

$$\cos\Psi = (\cos\alpha - \cos i\cos e)/\sin i\sin e \quad (20)$$

where $0 \le \Psi \le \pi$.

Hapke (1984) shows that the multiplicative factor, $S(i,e,\alpha)$ is given by:

$$S = (\mu'/u'^0)(\mu_0/\mu'^0_0)\frac{1}{\sqrt{1+\pi\tan^2\theta}} \left[1-f+\frac{f}{\sqrt{1+\pi\tan^2\theta}}(\mu_0/\mu'^0_0)\right]^{-1} \quad (21)$$

when $i \le e$ and by:

$$S = (\mu'/u'^0)(\mu_0/\mu'^0_0)\frac{1}{\sqrt{1+\pi\tan^2\theta}} \left[1-f+\frac{f}{\sqrt{1+\pi\tan^2\theta}}(\mu/\mu'^0)\right]^{-1} \quad (22)$$

when $i > e$. The function f is defined as the fraction of illumination shadow that overlaps with the visibility shadow for a particular facet. The illumination shadow, or tilt shadow, is the "shadow" a facet casts on itself such that the illumination source does not illuminate a portion of the surface due to its tilt. The visibility shadow, or projected shadow, is the "shadow" a facet casts on itself such that light reflected from its surface is angled away from the detector due to its tilt. This function is given as:

$$f = e^{-2\tan\frac{\Psi}{2}} \quad (23)$$

In addition, the cosines μ'^0_0 and μ'^0 are defined as:

$$\mu'^0_0 = \frac{1}{\sqrt{1+\pi\tan^2\theta}}\left(\cos i + \sin i\tan\theta\frac{e^{\frac{-\cot^2\theta\cot^2 i}{\pi}}}{2-e^{\frac{-2\cot\theta\cot i}{\pi}}}\right) \quad (24)$$

$$\mu'^0 = \frac{1}{\sqrt{1+\pi\tan^2\theta}}\left[\cos e + \sin e\tan\theta\frac{e^{\left(\frac{-\cot^2\theta\cot^2 e}{\pi}\right)}}{2-e^{\frac{-2\cot\theta\cot e}{\pi}}}\right]$$

Reflection by a smooth surface is given by:

$$r_s(i,e,\alpha) = \frac{\mu_0}{(\mu_0+\mu)}\left(\frac{w}{4\pi}\right) \{[1+B(\alpha)]P(\alpha)-1+H \quad (25)$$

$$(\mu_0)H(\mu)\}$$

(Hapke 1984, 1986), where $\mu_0 = \cos(i)$, $\mu = \cos(e)$, and H is the Chandrasehkar H function which Hapke (1984) approximates as:

$$H(x) = (1+2x)/[1+2x\sqrt{1-w}] \quad (26)$$

and which is used in these analyses as well.

Reflectance values along each segment of the crater profiles were calculated using these equations, where the dependence on incidence, emission, and phase angle are explicit. The code producing the reflectance values has been used to model disk-resolved data sets of Europa and terrestrial snows (Domingue and Hapke 1992; Domingue et al. 1997). The parameter values used are those listed in Table 5, based on the modeling of the lunar disk-integrated data.

SPECTRAL PHOTOMETRIC BEHAVIOR

Reflectance values were calculated at the wavelengths of the disk-integrated observations, producing a simulated spectrum for each segment along the crater profile at the latitude, longitude, and γ values discussed above. The spectra were normalized to 1.0 at 0.50 μm. Figure 4b shows examples of the normalized simulated spectra at 49° latitude, 75° longitude, and γ of 0°. The spectra shown are examples where the band at 0.86 μm is shallow (segment AU), deep (segment AZ), and of average depth (segment AH).

At the shorter wavelengths, no change in spectral slope is noted with changes in the illumination parameters. This is a common result at the shorter wavelengths for all of our simulations. Changes in reflectance with wavelength become apparent in the NIR wavelengths. Tables 7 through 11 show the percent variation in the spectral slopes between 0.50 and 0.63 μm and between 0.63 and 0.73 μm. The tables also list the percent variation in the continuum slope between 0.73 and 1.06 μm along with the percent variation in the 0.86 μm band depth. The percent variation is defined as the difference between the maximum and minimum values divided by the average value. The band depth is defined as the difference between the reflectance value modeled at 0.86 μm and the continuum value at 0.86 μm. The continuum 0.86 μm value was obtained from the equation of a line having a slope corresponding to the continuum slope and intercepting the normalized reflectance values at 0.73 and 1.06 μm. Those places in the tables labeled "n/a" indicate scenarios where no segments along the crater profile were illuminated.

Since the Hapke model has been shown to be predictive of reflectance behavior to within <2% (Cheng and Domingue 2000) for dark, lunar-like surfaces, any variation below 4% can be attributed to inaccuracies in the reflectance modeling. The tables show that there are some subtle variations in spectral slopes that are outside of the modeling errors. The most dramatic variation, however, is observed in the depth of the 0.86 μm band.

Figure 5 plots the normalized reflectance as a function of surface slope for each wavelength. These plots demonstrate that the wider range in variation is at longer wavelengths. However, these plots also show that there is a correlation between reflectance and surface slope at all wavelengths.

DISCUSSION OF OBSERVED SPECTRAL CHANGES

Variations in slope across the UV-VIS-NIR spectral region are present at levels ranging from those within the model inaccuracies (<4%) to levels just under 12%. Those

Table 7. Relative spectral slopes and band depths for γ = 0° orientation.

Latitude	Longitude	Slope (0.50 to 0.63)	Slope (0.63 to 0.73)	Slope (0.73 to 1.06)	0.86 band depth
49	10	7.47%	5.41%	6.62%	29.48%
	50	11.20%	8.26%	10.07%	58.49%
	75	11.61%	8.55%	10.41%	52.52%
	85	9.16%	6.77%	8.23%	51.77%
67	10	7.45%	5.44%	6.68%	69.68%
	50	9.78%	7.14%	8.73%	77.81%
	75	9.94%	7.26%	8.84%	82.97%
	85	10.26%	7.48%	9.12%	96.38%
80	10	4.69%	3.40%	4.16%	156.62%
	50	5.82%	4.22%	5.16%	146.28%
	75	6.33%	4.59%	5.61%	124.42%
	85	6.29%	4.56%	5.57%	110.21%
Min		4.69%	3.40%	4.16%	29.48%
Max		11.61%	8.55%	10.41%	156.62%

Table 8. Relative spectral slopes and band depths for γ = 60° orientation.

Latitude	Longitude	Slope (0.50 to 0.63)	Slope (0.63 to 0.73)	Slope (0.73 to 1.06)	0.86 band depth
49	10	4.38%	3.23%	3.95%	50.82%
	50	9.48%	7.04%	8.58%	123.44%
	75	8.03%	5.95%	7.27%	101.93%
	85	7.85%	5.81%	7.11%	88.25%
67	10	5.23%	3.87%	4.73%	93.70%
	50	10.43%	7.67%	9.38%	195.55%
	75	8.95%	6.60%	8.09%	148.64%
	85	8.51%	6.27%	7.69%	127.85%
80	10	8.61%	6.31%	7.73%	191.08%
	50	10.99%	8.03%	9.84%	265.49%
	75	10.36%	7.58%	9.29%	198.43%
	85	10.12%	7.42%	9.08%	163.57%
Min		4.38%	3.23%	3.95%	50.82%
Max		10.99%	8.03%	9.84%	265.49%

Table 9. Relative spectral slopes and band depths for γ = 90° orientation.

Latitude	Longitude	Slope (0.50 to 0.63)	Slope (0.63 to 0.73)	Slope (0.73 to 1.06)	0.86 band depth
49	10	5.44%	4.10%	5.03%	33.35%
	50	2.45%	1.90%	2.35%	52.86%
	75	5.00%	3.63%	4.45%	110.68%
	85	4.60%	3.38%	4.14%	21.90%
67	10	6.55%	4.91%	6.02%	64.01%
	50	4.33%	3.25%	3.99%	114.31%
	75	7.50%	5.45%	6.71%	305.70%
	85	6.90%	5.03%	6.19%	128.09%
80	10	8.31%	6.13%	7.54%	156.93%
	50	7.09%	5.25%	6.45%	273.22%
	75	9.38%	6.83%	8.41%	426.04%
	85	9.29%	6.78%	8.33%	292.42%
Min		2.45%	1.90%	2.35%	21.90%
Max		9.38%	6.83%	8.41%	426.04%

variations outside of the model inaccuracies are above those typically expected for a space-qualified spectral instrument. Changes in slope could be interpreted as an indicator of alteration processes (such as "space weathering"). In the example shown in Fig. 13, the slopes on segments G through AD ("left" wall of the crater profile) have a higher average slope than those associated with the segments on the "right" wall of the crater profile. If the photometric effects on spectral properties are not accounted for, this could lead to an erroneous interpretation of preferential alteration on one side of the crater compared to the other.

The variation in the depth observed in the 1.0 μm mafic silicate feature is significant. The greatest depth variation is seen at high latitudes. Thus, extremes in lighting conditions

Table 10. Relative spectral slopes and band depths for γ =130° orientation.

Latitude	Longitude	Slope (0.50 to 0.63)	Slope (0.63 to 0.73)	Slope (0.73 to 1.06)	0.86 band depth
49	10	5.26%	3.94%	4.82%	44.21%
	50	0.67%	0.53%	0.66%	13.45%
	75	n/a	n/a	n/a	n/a
	85	n/a	n/a	n/a	n/a
67	10	4.09%	3.06%	3.77%	3.13%
	50	1.03%	0.77%	0.95%	13.69%
	75	n/a	n/a	n/a	n/a
	85	n/a	n/a	n/a	n/a
80	10	2.16%	1.57%	1.93%	59.95%
	50	0.22%	0.16%	0.20%	17.30%
	75	n/a	n/a	n/a	n/a
	85	n/a	n/a	n/a	n/a
Min		0.22%	0.16%	0.20%	3.13%
Max		5.26%	3.94%	4.82%	59.95%

Table 11. Relative spectral slopes and band depths for γ = 180° orientation.

Latitude	Longitude	Slope (0.50 to 0.63)	Slope (0.63 to 0.73)	Slope (0.73 to 1.06)	0.86 band depth
49	10	3.10%	2.31%	2.84%	14.85%
	50	0.31%	0.22%	0.25%	15.06%
	75	n/a	n/a	n/a	n/a
	85	n/a	n/a	n/a	n/a
67	10	0.17%	0.11%	0.13%	86.37%
	50	0.11%	0.07%	0.09%	28.85%
	75	n/a	n/a	n/a	n/a
	85	n/a	n/a	n/a	n/a
80	10	0.34%	0.25%	0.30%	136.31%
	50	0.02%	0.01%	0.01%	52.73%
	75	n/a	n/a	n/a	n/a
	85	n/a	n/a	n/a	n/a
Min		0.02%	0.01%	0.01%	14.85%
Max		3.10%	2.31%	2.84%	136.31%

artificially enhance the strength of an existing spectral reflectance absorption feature. This is true even though the slope of the background continuum on which this absorption feature is superimposed does not change as significantly. This affects different methods of interpreting the data, including the computation of 1.0 μm mafic silicate feature band area, fitting the 1.0 μm mafic silicate feature band with a Gaussian function, or directly comparing the absorption with laboratory or remotely sensed spectra. Data acquired under extreme photometric conditions (e.g., high latitudes) will require modeling the correction needed to analyze the mineralogical composition quantitatively. Changes in band depth can be interpreted as an indicator of compositional change (either change in relative abundance, or the addition of an absorber) or textural changes (such as particle size variation). In the example shown in Fig. 13, the band depth on segments G through AD ("left" wall of the crater profile) have a higher average slope than those associated with the segments on the "right" wall of the crater profile, which is similar to what is seen in the slope values. If the photometric effects on spectral properties are not accounted for, this could lead to an erroneous interpretation of compositional or textural differences on one side of the crater compared to the other. Within the gross spectral resolution of our study, we see no evidence for a change in band center for the 1.0 μm mafic silicate feature; however, at this resolution, a change in band center could manifest itself as a change in band depth. The data do not allow us to discriminate between the two. Finer resolution would further address this issue.

One effect of topography, which is not directly addressed by this study, is that of "stray light." Stray light is defined as light that is either scattered from a surface outside the instrument field of view (FOV) into the FOV and onto the detector, or light that is scattered from a surface facet outside the FOV onto a second surface facet in the FOV and onto the detector. For spatially-resolved observations, local topography can be a source of stray light, or light that is captured by an instrument from terrain outside of the FOV of the instrument (cf. Gaddis et al. 1995, 1996). (This effect should be distinguished from scattered light due to internal reflections within the optical system itself.) At present, there is no method for removing the effects of stray light from spatially resolved spacecraft spectral or imaging data; the effects of this underlying additive light component need to be understood in order to calibrate or interpret spacecraft data correctly.

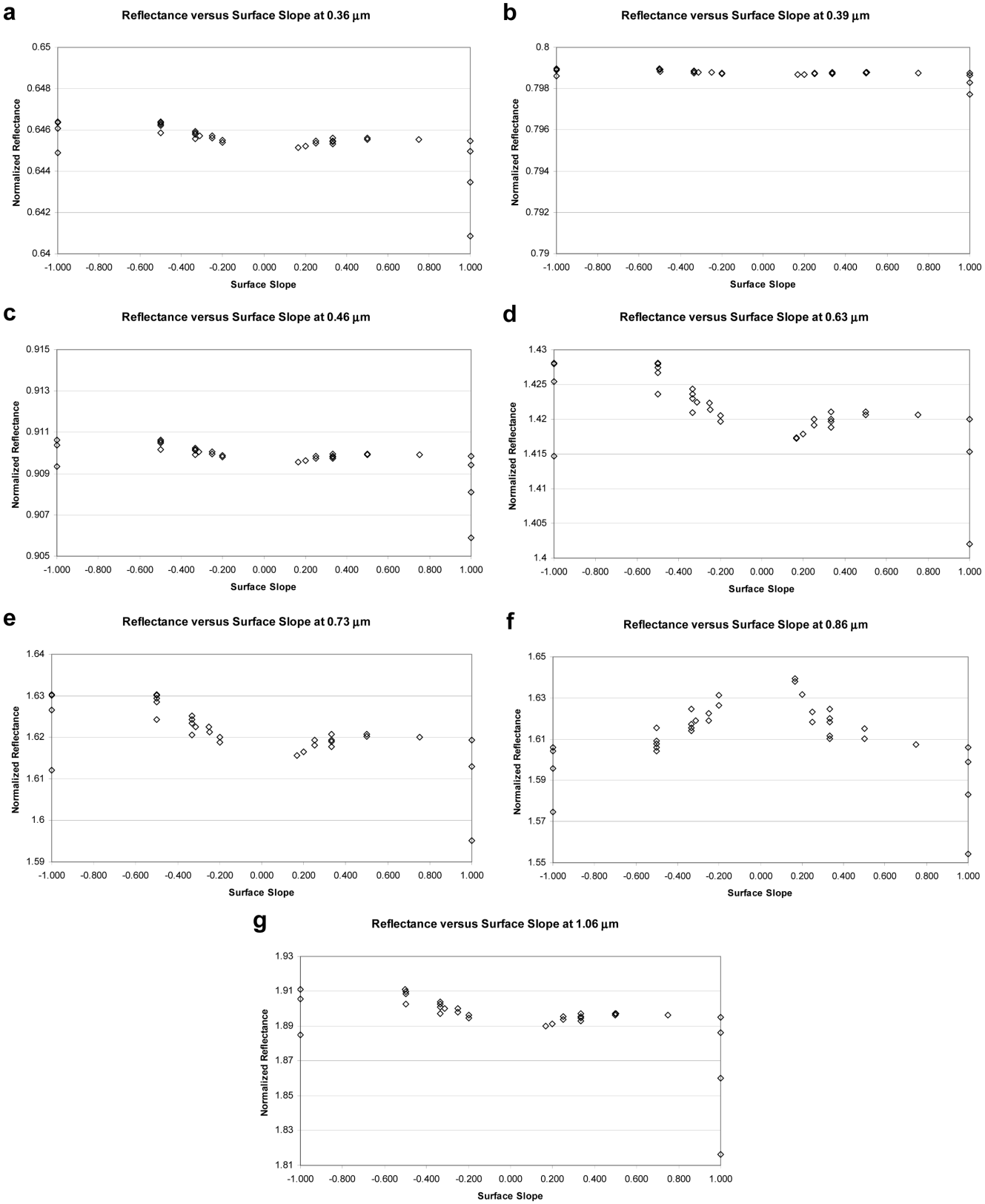

Fig. 5. Plots of normalized reflectance (at 0.50 µm) versus surface slope at (a) 0.36 µm, (b) 0.39 µm, (c) 0.46 µm, (d) 0.63 µm, (e) 0.73 µm, (f) 0.86 µm, and (g) 1.06 µm. The largest variations are seen at longer wavelengths, but all wavelengths show a similar correspondence between reflectance and surface slope.

The history of spacecraft observations includes many examples of the effects of stray light where topography is suspected of being the cause. Gaddis et al. (1995, 1996) observe a residual brightness due to stray light after carefully removing the scattered light component from partial-disk images of the Moon taken during the two Galileo Earth-Moon passes. They used whole-disk images from both fly-bys for their study of scattered light removal calibration, where scattered light was expected to be the only contribution to any additive light component. In a study of the central peaks of lunar craters, Tompkins and Pieters (1999) note that Clementine imaging data acquired at very high phase angles of these steeply sloped surfaces can appear up to 20% brighter than any known lunar materials. The increased brightness of these central peak walls was ascribed to added illumination of these surfaces from light scattered off the surrounding terrain (such as the crater walls). As a result, they limit their compositional interpretations of craters at latitudes greater than ±60° (nearer the poles). However, our results indicate that it is also possible to ascribe part of the increased brightness of the central peak walls to photometric effects induced by the terrain.

This study shows that, for this level of spectral resolution (which is typical of spacecraft imaging data), no false absorption feature due to wavelength-dependent changes in reflectance is created by the topographic effects on the photometry. Thus, spectral data containing stray light from outside the instrumental FOV (assuming the material outside the FOV is of the same composition), which was captured after being reflected through large surficial angles, will not show spurious absorption features. (This study also does not address the percentage of the total I/F that can be attributed to stray light.) Higher spectral resolution data may yet show that band centers may shift as a function of viewing geometry, which leaves open the possibility for producing spurious features. However, this study does demonstrate that at resolutions typical of planetary imagers, spurious features are not created.

IMPLICATIONS FOR GROUND-BASED AND SPACECRAFT OBSERVATIONS OF THE MOON (AND PROBABLY MERCURY)

While the implications of this study potentially extend to rocky surface regoliths of different compositions, this study primarily addresses effects of underlying topography on photometry and spectroscopy of the lunar surface. Many lunar spacecraft missions planning UV-VIS-NIR spectroscopy are currently under development or in flight. The European Space Agency (ESA) currently has the SMART-1 spacecraft in lunar orbit, which includes a panchromatic camera and a visible/infrared spectrometer in its payload. The Japanese Space Agency (JAXA) launched the Selenological and Engineering Explorer (SELENE) in 2007, which has a multiband imager and a spectral profiler in its payload. The Indian Space Research Organization (ISRO) is preparing to launch Chandrayaan-1 in 2008. This mission will include the Hyper Spectral Imager (HySI) and the Moon Mineral Mapper (M^3) in its payload. Another lunar mission launched in 2007 is the Chinese Chang'e 1, which includes a camera system in its payload. In 2008, NASA plans to launch the Lunar Reconnaissance Orbiter (LRO), which will include a high-resolution camera. Ground-based observations in support of these missions should consider the effects on spectroscopy of the underlying topography.

By comparison, the surface of Mercury is expected to be similar in composition to the Moon (cf. Vilas 1988; Sprague et al. 2002; Warrell et al. 2006). Currently, the NASA Discovery mission MESSENGER is en route to a 2008 fly-by encounter with Mercury (with a 2011 orbit insertion), while ESA is planning the Cornerstone mission Bepi Colombo to follow with a surface lander. Mercury's close proximity to the Sun, coupled with the quasicommensurability in its orbital period, subjects the planet to high and low temperature extremes. Studies suggest that the high temperatures will broaden the widths and shift band centers to lower wavelengths (higher energies) of absorption features in the observed reflectance spectra due to increased vibrational disorder (cf. Singer and Roush 1985; Lucey et al. 2002), and could invoke a latitudinally dependent change due to the Ostwald effect (Noble and Pieters 2003). The increase in micrometeoroid impacts caused by the focusing of material in the gravitational well (Cintala 1992) will increase the alteration of the surface material ("weathering") by those repeated impacts. With the interest in the Mercurian high latitude regions prompted by the radar-bright craters, spectral observations of the polar regions is of great interest; these regions, of course, are subject to photometric extremes created by the illumination of variable topography. The presence or absence of the 1.0 μm mafic silicate feature in ground-based spectra is debated (e.g., Vilas 1988), and modeling the effects of topography on photometry and spectroscopy of Mercury's surface will be an important part of the data analysis.

SUMMARY

Using disk-integrated photometric observations of the Moon obtained across eight broadband filters ranging from 0.36 to 1.06 and covering a range of phase angles from 6 to 120 degrees, we modeled the lunar photometric function at each wavelength using a modified Hapke model. We then used these models to explore the change in lunar spectral properties under varying lighting conditions invoked by the surface topography and illumination angles. The changes that we have seen as part of this study are significant for both what we have observed and what we have not observed. We find that both the underlying spectral slope and the depth of the

1.0 μm mafic silicate feature change under varying lighting conditions, although to different degrees. Due to the spectral resolution, there is no description of any variations in the band centers due to variations in lighting conditions. The effects of the underlying topography are most pronounced for changes in depth of the 1.0 μm mafic silicate absorption feature. These changes could be sufficient to change the interpretation of the mineral abundance being observed. While the characteristics of existing spectral absorption features can be enhanced, we see no evidence for the generation of false spectral absorption features due to lighting extremes caused by underlying topography, though this may be a spectral resolution effect. Based on these results, however, we do not expect the generation of false spectral absorption features from varying lighting conditions. Regardless, future disk-resolved observations of the Moon and the planet Mercury will benefit from consideration, and probable removal, of these effects before mineralogical interpretation.

Acknowledgments–Deborah Domingue acknowledges support from the NEAR Data Analysis Program (NAG512646) and Discovery Program MESSENGER (NAS5-97271) for this work. Faith Vilas acknowledges the NASA Lunar Data Analysis Program.

Editorial Handling—Dr. Michael Gaffey

REFERENCES

Buratti B. J., Hillier J. K., and Wang M. 1996. The lunar opposition surge: Observations by Clementine. *Icarus* 124:490–499.

Cheng A. F. and Domingue D. L. 2000. Radiative transfer models for light scattering from planetary surfaces. *Journal of Geophysical Research* 105:9477–9482.

Cintala M. J. 1992. Impact-induced thermal effects in the lunar and Mercurian regoliths. *Journal of Geophysical Research* 97:947–973.

Domingue D., Hartman B., and Verbiscer A. 1997. The scattering properties of natural terrestrial snows versus icy satellite surfaces. *Icarus* 128:28–48.

Domingue D. and Hapke B. 1992. Disk-resolved photometric analysis of Europan terrains. *Icarus* 99:70–81.

Domingue D. and Vilas F. 2005. Spectral photometric properties of the Moon (abstract #1978). 36th Lunar and Planetary Science Conference. CD-ROM.

Gaddis L., McEwen A. S., and Becker T. 1996. Analyses of Galileo SSI data from EM2: Scattered light effects (abstract). 7th Lunar Science Conference. pp. 387–388.

Gaddis L., McEwen A. S., and Becker T. 1995. Recalibration of Galileo SSI lunar data from EM1: The effects of scattered light removal (abstract). 26th Lunar and Planetary Science Conference. pp. 435–436.

Gehrels T. 1967. Minor planets. IL photographic magnitudes. *The Astronomical Journal* 72:1288–1291.

Hapke B. 1981. Bidirectional reflectance spectroscopy. 1. Theory. *Journal of Geophysical Research* 68:4571–4586.

Hapke B. 1984. Bidirectional reflectance spectroscopy. 3. Correction for macroscopic roughness. *Icarus* 59:41–59.

Hapke B. 1986. Bidirectional reflectance spectroscopy. 4. The extinction coefficient and the opposition effect. *Icarus* 67:264–280.

Hapke B. 2002. Bidirectional reflectance spectroscopy. 5. The coherent backscatter opposition effect and anisotropic scattering. *Icarus* 157:523–534.

Hapke B., Nelson R., and Smythe W. 1998. The opposition effect of the Moon: Coherent backscatter and shadow hiding. *Icarus* 133: 89–97.

Hartman B. and Domingue D. 1998. Scattering of light by individual particles and the implications for models of planetary surfaces. *Icarus* 131:421–448.

Helfenstein P. and Shepard M. K. 1999. Submillimeter-scale topography of the lunar regolith. *Icarus* 141:107–131.

Helfenstein P. and Veverka J. 1987. Photometric properties of lunar terrains derived from Hapke's equation. *Icarus* 72:342–357.

Helfenstein P., Veverka J., and Hillier J. 1997. The lunar opposition effect: A test of alternative models. *Icarus* 128:2–14.

Helfenstein P., Veverka J., Thomas P. C., Simonelli D. P., Lee P., Klaasen K., Johnson T. V., Breneman H., Head J. W., and Murchie S. 1994. Galileo photometry of asteroid 951 Gaspra (abstract). *Icarus* 107:37.

Hillier J. K., Buratti B. J., and Hill K. 1999. Multispectral photometry of the Moon and absolute calibration of the Clementine UV/VIS camera. *Icarus* 141:205–225.

Irvine W. M., Simon T., Menzel D. H., Pikoos C., and Young A. T. 1968. Multicolor photoelectric photometry of the brighter planets. III. Observations from Boyden Observatory. *The Astronomical Journal* 73:807–828.

Johnson P. E., Smith M. O., and Adams J. B., 1992. Simple algorithms for remote determination of mineral abundances and particle sizes from reflectance spectra. *Journal of Geophysical Research* 97:2649–2657.

Johnson P. E., Smith M., Taylor-George S., and Adams J. B. 1983. A semiempirical method for analysis of the reflectance spectra of binary mineral mixtures. *Journal of Geophysical Research* 88: 3557–3562.

Kieffer H. H. and Stone T. C. 2005. The spectral irradiance of the Moon. *The Astronomical Journal* 129:2887–2901.

Korokhin V. V. and Velikodsky Yu. I. 2005. The spectral irradiance of the Moon (abstract #1437). 36th Lunar and Planetary Science Conference. CD-ROM.

Lane A. P. and Irvine M. 1973. Monochromatic phase curves and albedos for the lunar disk. *The Astronomical Journal* 78:267–277.

Lucey P. G., Hinrichs J., Kelly M., Wellnitz D., Izenberg N., Murchie S., Robinson M., Clark B. E., and Bell J. F. III. 2002. Detection of temperature-dependent spectral variation on the asteroid Eros and new evidence for the presence of an olivine-rich silicate assemblage. *Icarus* 155:181–188.

Mustard J. F. and Pieters C. M. 1989. Photometric phase functions of common geologic minerals and applications to quantitative analysis of mineral mixture reflectance spectra. *Journal of Geophysical Research* 94:13,619–13,634.

Noble S. K. and Pieters C. M. 2003. Space weathering on Mercury: Implications for remote sensing. *Solar System Research* 37:31–35.

Nygard S. 1975. Alpha Lyrae/Sun flux ratios for use in standard star calibrations: Results of three techniques. M.Sc. thesis, Massachusetts Institute of Technology, Cambridge, Massachusetts, USA.

Rougier M. G. 1933. Total photoelectric photometry of the Moon. *Annals of Strasbourg Observatory* 2:205–339.

Russell H. N. 1916a. On the albedo of planets and their satellites. *The Astrophysical Journal* 43:173–197.

Russell H. N. 1916b. The stellar magnitudes of the Sun, Moon, and planets. *The Astrophysical Journal* 43:103–129.

Shorthill R. W., Saari J. M., Baird F. E., and LeCompte J. R. 1969. Photometric properties of selected lunar features. NASA Contractor Report CR-1429. Washington, D.C.: National Aeronautics and Space Administration.

Singer R. B. and Roush T. L. 1985. Effects of temperature on remotely sensed mineral absorption features. *Journal of Geophysical Research* 90:12,434–12,444.

Sprague A. L., Emery J. P., Donaldson K. L., Russell R. W., Lynch D. K., and Mazuk A. L. 2002. Mercury: Mid-infrared (3–13.5 μm) observations show heterogeneous composition, presence of intermediate and basic soil types, and pyroxene. *Meteoritics & Planetary Science* 37:1255–1268.

Sunshine J. M., Pieters C. M., and Pratt S. F. 1990. Deconvolution of mineral absorption bands—An improved approach. *Journal of Geological Research* 95:6955–6966.

Tompkins S. and Pieters C. M. 1999. Mineralogy of the lunar crust: Results from Clementine. *Meteoritics & Planetary Science* 34: 25–41.

Vilas F. 1988. Surface composition of Mercury from reflectance spectrophotometry. In *Mercury,* edited by Vilas F., Chapman C., and Matthews M. Tucson, Arizona: The University of Arizona Press. pp. 59–76.

Warell J., Sprague A. L., Emery J. P., Kozlowski R. W. H., and Long A. 2006. The 0.7–5.3 μm IR spectra of Mercury and the Moon: Evidence for high-Ca clinopyroxene on Mercury. *Icarus* 180:281–291.